Evaluation of a Cartesian-Grid Based Numerical Method for Flow over Sphere

By

Mohamed Y. A. Salem

A Thesis
Submitted to the Faculty of Graduate Studies
In Partial Fulfillment of the requirements for the Degree of

Master of Science
In
Mechanical Engineering

Department of Mechanical and Manufacturing Engineering
The University of Manitoba
Winnipeg, Manitoba
Canada

Evaluation of a Cartesian-Grid Based Numerical Method for Flow over Sphere

BY

Mohamed Y. A. Salem

A Thesis/Practicum submitted to the Faculty of Graduate Studies of The University of Manitoba in partial fulfillment of the requirement of the degree

MASTER OF SCIENCE

ABSTRACT

This thesis presents an evaluation of a numerical method for predicting flow characteristics over a sphere. This numerical method, which is proposed by Birouk and Abou Al-Sood (2007), is a Cartesian based-grid which employs a blocked-off treatment of the sphere to solve for the surrounding flow. The steady-state three-dimensional continuity and momentum equations are solved. Closure for the turbulence stress terms in the flow momentum equations are handled by using the standard k-ε model or shear stress transport (SST) model. To evaluate the accuracy of this method, its predictions are compared with those obtained by using a different numerical approach, which is a conventional method implemented in the CFD code Fluent. Note that the only difference between these two numerical methods is the way the sphere is treated in the computational domain. The sphere surface profile appears as step stairs with the Cartesian grid-based blocked-off technique, whereas the profile of the sphere surface is nearly preserved when using the conventional method. The two different methods are found to produce similar predictions, which is an indication of the ability of the new method for generating quality data.

ACKNOWLEDGEMENTS

I would like to deeply thank the various people who, during this endeavor of this thesis, provided me with useful and helpful assistance. Without their care and consideration, this thesis would likely not have matured. I would like to express my profound gratitude to my supervisor, Dr. Madjid Birouk, who stood by me all the time and guided and encouraged me to the achievement of this work. His unending concern for through job and sustained guidance and encouragements are greatly appreciated.

My thanks also go to my research group: Maher Abou Al-Sood, Kevin Khadami, Mohamed Zakaria, and Christopher Iyogun who spent considerable time helping with Gambit, Fluent, and giving constructive criticisms. Their help through this work has been valuably productive. I would like finally to thank the Libyan Embassy for the support that has been granted to me during the whole time of my research.

TABLE OF CONTENTS

LIST OF FIGURES

LIST OF TABLES

NOMENCLUTURE

ROMAN LETTERS

C_p	pressure coefficient
C_D	drag coefficient
C_μ	constant
C_2	empirical constant
d	diameter
f_μ	damping function
I	turbulence intensity (u' / U_∞)
k	turbulence kinetic energy
L_t	integral length scale
l_m	mixing length scale
P	pressure
r	radius
n	normal direction to the wall
Re	Reynolds number
S_Φ	source term ($S_\Phi = S_c + S_p \Phi$)
U	mean-velocity component in x-direction
u'	fluctuation velocity component in x-direction
$\overline{u_i u_j}$	Reynolds stresses
V	mean-velocity in y-direction
V	volume
W	mean-velocity in z-direction
x	coordinates

GREEK LETTERS

ϕ	azimuthal angle
Φ	diffusion parameter (u, v, w, p, k, ε, ω)
ρ	density
ω	dissipation per unit turbulence kinetic energy
ν	kinematic viscosity
ν_t	eddy viscosity
μ	molecular viscosity
τ	shear stress
τ_{ij}	shear stress tensor
Γ	generalized diffusion coefficient
ε	turbulence dissipation rate

μ_t turbulence viscosity

δ_{ij} Kronecker delta

SUBSCRIPTS

B	bottom $(i, j, k\text{-}1)$ node
E	east $(i\text{+}1, j, k)$ node
N	north $(i,j\text{+}1,k)$ node
P	center (i, j, k) node
S	south $(i, j\text{ -}1, k)$ node
T	top $(i, j\text{ , }k\text{ +}1)$ node
W	west $(i\text{ -}1, j, k)$ node
∞	freestream

Chapter 1

INTRODUCTION

Flow over a spherical object, whether an evaporating droplet or a non-evaporating droplet (solid sphere or particle), is a phenomenon encountered in numerous industrial fluid flow processes. This would include the vaporization and combustion of spray, air cleaning devices, centrifugal or sedimentation separators, fluidized-bed reactors, etc. Therefore, knowledge of the overall dynamics of the flow around a spherical object is essential for the design and performance of such industrial processes. Details/knowledge of the flow field can in general be gained by performing a physical experiment or a numerical simulation. Unlike the experiment, the numerical simulation if validated is generally cost effective in terms of time and required recourses.

Some numerical studies employed the assumption of axisymmetric flow over a sphere; see for example, Fornberg (1988), although the flow is three-dimensional (3D). This assumption is particularly due to difficulties in creating a 3D computational grid especially in spherical coordinates. However, in recent years several attempts have been made to overcome this difficulty; see, for example, Johnson and Patel (1999), Constantinescu and Squires (2004), Niazmand and Renksizbulut (2005), Kim *et al.* (2001), and Abou Al-Sood (2006). This is achieved, for example, by transforming Navier-Stokes equations coordinates from spherical into another type of simpler coordinates (ξ, η, and ζ) which enable using

Cartesian grid (Johnson and Patel, 1999). This approach, in fact, makes the discretization process (the transformation of governing flow differential equations into algebraic form) quite complicated when using finite-volume scheme. Other approaches use immersed-boundary fitted method, which is based on introducing a virtual body into the flow field of interest (e.g., Kim *et al.,* 2001). The use of a virtual body, which is a sort of momentum forcing in the Navier-Stokes equations, allows employing Cartesian or cylindrical grid.

Recently, Birouk and co-workers attempted, for the first time, to employ a much simpler method (Birouk and Abou Al-Sood, 2007; Abou Al-Sood, 2006; Abou Al-Sood and Birouk, 2008). It is termed blocked-off technique. It consists of using a calculation Cartesian grid-based domain that includes both the gas and non-gaseous (sphere or liquid droplet) phases, in which the solution is obtained by blocking off the control volumes of the inactive phase when solving for the active phase. It is important to mention that the blocking-off procedure was first developed to compute flows in curvilinear geometries with a regular grid, as well as to solve conjugate heat transfer problems in ducts (e.g., Patankar, 1978 and 1991). It was successfully extended to solve radiative heat transfer problems in irregular two-dimensional geometries using Cartesian coordinates (e.g., Chai *et al.*, 1993; Kim *et al.*, 2001; Byun *et al.*, 2003). It is only recently that it has been used to solve flow problems in enclosures with obstacles that are three-dimensional problems (e.g., Coelho *et al.*, 1998; Borjini *et al.*, 2003; Consalvi *et al.*, 2003).

The blocked-off method may be considered advantageous over the aforementioned techniques due to its simplicity, and easiness for grid generation

and implementation compared to unstructured or multi-block grid generation, while it still able to produce quality predictions. Although the recent work showed that this relative simple procedure cannot capture the exact/real surface profile of the spherical object (as it can be seen in chapter 3), reasonably good predictions were obtained when compared to experiments (Birouk and Abou Al-Sood, 2007). This, in fact, is achieved by using a very fine grid, which of course would increase the CPU time. However, the degree of inaccuracy of this method is still unknown, as several parameters depend upon the shape of the spherical object surface. The present work aims at verifying the accuracy of the predictions of this method. This is achieved by employing another different independent numerical technique that is capable of preserving the real sphere surface profile. The full thesis will present and discuss, as example, the mean drag coefficient of sphere in laminar and turbulent flows, as predicted by both different methods.

The thesis is organized as follows. The pertinent literature survey is presented in the next chapter, followed by the mathematical formulation of the numerical models. Results and discussion are presented in chapter 5, and a short conclusion is provided in chapter 6.

Chapter 2

LITERATURE REVIEW

Various numerical techniques have been used to study the behaviour of a flow over a sphere (e.g., Fornberg, 1988; Johnson and Patel, 1998; Satoshi *et al.*, 1999; Constantinescu and Squires, 1999; 2003; 2004; Fadlun *et al.*, 2000; Kim *et al.*, 2001; Constantinescu *et al.*, 2002; Gilmanov *et al.*, 2003; Bagchi and Balachandar, 2003; Constantinescu *et al*, 2003; Wang and Kannan, 2005; and Birouk and Abou Al-Sood, 2007). Although, the flow field around a sphere is known to be complex and possesses several features that are difficult to capture, the majority of these techniques produced results that are in agreement with one another, as well as with published experimental data (e.g., Torobin and Gauvin, 1961; Clamen and Gauvin, 1969; Uhlherr and Sinclair, 1970; Ross and Willmarth, 1971; Zarin and Nicholls, 1971; Anderson and Uhlherr, 1977; Schlichting, 1979; Neve, 1986; Ruddolff and Bachalo, 1988; Clift and Grace, 1989; Gore and Growe, 1990; Warnica *et al.*, 1995a; Yusof, 1996; and Brucato *et al.*, 1998).

Fornberg (1988) developed a numerical technique to study the flow over a 1 mm diameter sphere at high Reynolds numbers up to 5000. His technique was based on conformal mapping. It maps the computational domain for the physical $(X = x + iy)$-plane to a rectangular $(Z = \xi + i\eta)$-plane. Fornberg (1988) used centered-order finite differences (Newton's method) to approximate the governing equations for all inner points of the computational domain.

Johnson and Patel (1998) investigated numerically steady and unsteady laminar flow of incompressible viscous fluid past a sphere at Reynolds numbers ranging up to 300. Their grid was an O-O type where the numerical coordinates (ξ,η,ζ) lie along the standard spherical coordinates (θ,ϕ,r). Dual-time-stepping and local pseudo-time stepping formulations were incorporated. They used a four-stage Runge-Kutta method to solve the momentum equations in pseudo-time. Also, a pressure Poisson equation was formulated to satisfy the continuity equation. By following a spherical coordinate system, the sphere lends itself naturally to the generation of the numerical grid.

Satoshi *et al.* (1999) developed a new numerical scheme for the use of direct numerical simulation to study a laminar flow over a sphere. The sphere was several times larger than the spacing of the computational domain. They used finite-difference method to simulate the flow field with a fixed grid system Cartesian coordinates. The basic equations (mass, conservation equation and Navier-Stokes equations) were discretized by employing a staggered arrangement on the grid system in Cartesian coordinates. The grid spacing in each direction of the field was uniform but it was not a condition of the scheme. In the region close to the particle (i.e. sphere), they used a third order interpolation (i.e. Cubic-Interpolated Pseudo-Particle (CIP) method). However, the calculation of the transport equation for velocity gradient was reduced in order to minimize the computing resources.

Constantinescu and Squires (1999) applied Large Eddy Simulation (LES) and Detached Eddy Simulation (DES) to investigate a turbulent flow around a sphere at a Reynolds number Re = 10^4. They performed their calculations in the sub-critical

regime (laminar boundary layer separation) by using a mesh of an O-type. The flow governing equations were solved using the partial transformation approach. Using a fully-implicit fractional-step algorithm, the momentum and turbulence-model equations were integrated over a pseudo-time approach. Fifth-order upwind difference method was used to discretize the convective terms in the momentum and turbulence transport equations near the sphere surface, while a second-order central difference method was used in the sphere wake region.

Fadlun *et al.* (2000) used the immersed-boundary technique to simulate unsteady three-dimensional incompressible flows in complex geometries including sphere. This was achieved by using boundary body forces that allow the imposition of the boundary conditions on a given surface not coinciding with the computational grid. A regular mesh was used to solve the discretized governing equations. Two different forcings were tested and it was shown that the quality of the results didn't change in both cases. One of the disadvantages of this method is that the interpolation of the forcing over the grid determines the accuracy of the scheme.

Kim *et al.* (2001) developed an immersed-boundary method for simulating flows over complex geometries (i.e. sphere and circular cylinder) where they introduced a mass source as well as a momentum forcing. A finite-volume approach is applied on a staggered mesh together with a fractional-step method. To satisfy the no-slip boundary condition on the immersed boundary, both momentum forcing and mass source were applied on the body surface or inside the body. The reason for that was to satisfy the continuity of the cell containing the immersed boundary. They applied momentum forcing when the forcing point coincides with the immersed boundary

so that the velocity is considered to be zero at that point. However, they applied the momentum forcing when the forcing point exists inside the body so that the velocity is the opposite of that outside the body for both velocity components (the wall-normal and tangential). In this method, the body in the flow field was considered as a kind of momentum forcing in the Navier-Stokes equations rather than a real body. Therefore, flow over complex geometries can easily be handled by using orthogonal (Cartesian or cylindrical) grids which generally do not coincide with the body surface.

Constantinescu *et al.* (2004) applied Detached-Eddy Simulation (DES) to investigate turbulent flow around sphere over a range of Reynolds numbers ranging from 10^4 to 1.1×10^6. A modification of the Spalart-Allmaras one-equation model was used to develop their formulation. It is reported that Detached-Eddy Simulation is a technique that is computationally feasible when predicting the flow for high Reynolds numbers (Constantinescu *et al.*, 2004). It also has the ability to resolve time dependent and three-dimensional turbulent motions. In their study, DES was applied to predict a flow around a sphere for both sub-critical and super-critical regimes (i.e. laminar and turbulent layer boundary separation, respectively). The initial and boundary conditions of the simulations were used to specify the laminar or turbulent boundary layer. A fractional step method was used to compute the incompressible flow over the sphere. The momentum and turbulence transport equations were discretized using fifth-order accurate upwind differences for the convective terms. All other operators were discretized using second-order central differences. The numerical method was fully implicit and the equations were solved on a simple O-O grid with the radial, polar, and azimuthal directions in a domain

that extended from $r = 0.5D$ (where D is the sphere diameter) to 10 diameter in the radial direction.

Gilmanov *et al.* (2003) investigated incompressible flow with complex immersed boundaries by using a general reconstruction algorithm in Cartesian grid. They used an unstructured triangular mesh to disctretize the three-dimensional solid surface that is immersed in the fluid. They were able to identify all the Cartesian grid nodes near the interface. The reconstruction of the solution in these nodes was obtained via linear interpolation along the local normal to the body, in a way that the desired boundary conditions for both pressure and velocity fields were enforced. On non-staggered grids, the three-dimensional, incompressible Navier-Stokes equations were solved using a second-order, finite difference approach. The three-point central differencing method was used to discretize the governing equations. The second-order accurate QUICK upwind scheme was used for the convective terms. They used the second-order accurate, dual time stepping, artificial compressibility approach for integrating the discrete equations in a time-accurate manner.

Bagchi and Balachandar (2003) applied a direct numerical simulation (DNS) to study the effect of freestream isotropic turbulent flow on the drag and lift forces of a micro (spherical) particle. Their test conditions include a Reynolds number ranging from 60 to 600 and freestream turbulence intensity from 10 to 25%. They solved the governing (continuity and Navier-Stokes) equations by a direct numerical simulation in a spherical domain attached to the particle. A Fourier-Chebyshew collocation scheme in spherical coordinates was used for the spatial discretization. Also a two-step time-split scheme was used for the temporal discretization, and a

non-reflecting boundary condition was used at the outflow boundary of the spherical domain. No-slip and no-penetration conditions were satisfied on the surface of the particle. The distribution of the grid points in the domain was nonuniform, that is clustered near the surface of the particle and in the wake region. The grid generated was adequate to resolve the thin shear layers and the wake structures generated by the particle.

Constantinescu *et al.* (2003) studied the incompressible flow over a sphere by applying unsteady Reynolds-averaged Navier-Stokes (URANS) equations. The predictions of URANS were obtained by using two layer $k-\varepsilon$, $k-\omega$, v^2-f, and the Spalart-Allmaras model. In their study, a fractional step method was used to compute the flow around the sphere. They transformed the governing equations to the generalized curvilinear coordinates with the primitive velocities and pressure were both kept as the dependent variables. The momentum and turbulence model equations were integrated in pseudo time using a fully implicit algorithm. In the first step of the fractional step method, an intermediate velocity field was obtained by advancing the convection and diffusion terms. That was done by using an alternate direction implicit approximate factorization scheme. The intermediate field was obtained with the current pressure field and does not satisfy the continuity equation. Therefore, a Poisson equation was solved for the pressure, for which the resulting solution was used to update the intermediate velocities to satisfy the continuity equation. Local time-stepping techniques were used to accelerate the convergence of the resulting system of equations. The source terms in the turbulence-model equations were also treated implicitly.

Wang and Kannan (2005) used an overset adaptive Cartesian/prism grid method to compute the moving boundary flow over a sphere. Their technique enabled avoiding grid remeshing when dealing with moving boundary flow problems. They used an adaptive Cartesian grid for moving boundary problems as the Cartesian cells are more efficient in filling space than triangular/tetrahedral. Also, solutions based on geometry-based grid adaptations are straightforward to carry out. In their method, body-fitted prism grids were generated first near solid bodies to resolve viscous boundary layer. Whereas an adaptive Cartesian grid is used to cover the outer domain and serve as the background grid for bridging the gaps between the prism grids. The prism grids are used to generate holes in the adaptive Cartesian grid to facilitate data communications.

Birouk and Abou Al-Sood (2007) developed a simple numerical technique to investigate numerically the effect of freestream turbulence intensity on the drag coefficient of a sphere immersed in a turbulent airstream for Reynolds numbers ranging between 10 and 250 and freestream turbulence intensity up to 60%. The three-dimensional Reynolds-Averaged Navier-Stokes (RANS) equations along with mass conservation were solved in Cartesian coordinates by using a blocked-off method. Although this method is very simplistic compared to all techniques mentioned above, it generated results that are fairly comparable with published data. The only disadvantage of this technique is its inability to configure the exact shape of the sphere (discussed in the next chapter). However, turbulence results appeared to depend upon the RANS turbulence closure models, for which their predictions are thought to be possibly related to the step stairs shape of the sphere which is imposed by this technique. Therefore, the ultimate objective of this thesis

is to use a different/independent technique which enables capturing the exact sphere surface shape to evaluate the degree of accuracy of the predictions of the blocked-off technique.

Chapter 3

PROBLEM DESCRIPTION AND MATHEMATICAL FORMULATION

3.1 Description of the Physical Problem

A stationary sphere of 1mm radius immersed into a turbulent freestream of infinite expanse is considered. The freesteam is prescribed by a mean-velocity, U_∞, a turbulence intensity, I_∞, a pressure P_∞, a kinetic energy, k_∞, and a turbulence dissipation rate, ε_∞, or turbulence dissipation rate per unit of turbulence kinetic energy, ω_∞. The flow over the sphere is assumed to be steady, turbulent with no heat transfer from/to the sphere, and the sphere remains stationary all the time. The stationary sphere of a radius of 1 mm exposed to turbulent airstream is schematically shown in Figure 3.1.

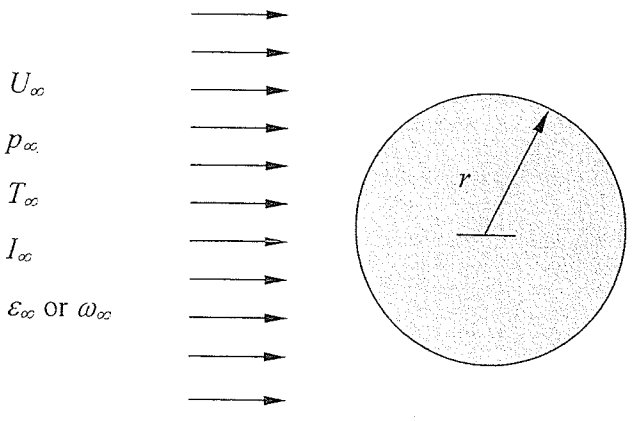

Fig. 3.1 Schematic of a stationary sphere, of radius r, exposed to a cross airstream

3.2. Governing Equations

The governing equations (which are the steady state, three dimensional, mass conservation and Reynolds-Averaged Navier-Stokes (RANS) equations) for a turbulent flow over a sphere can be written as

$$\frac{\partial}{\partial x_i}(\rho U_i) = 0, \tag{3.1}$$

$$\frac{\partial}{\partial x_j}(\rho U_i U_j) = -\frac{\partial p}{\partial x_i} + \frac{\partial}{\partial x_j}\left(\mu \frac{\partial U_i}{\partial U_j} - \overline{\rho u_i' u_j'}\right), \tag{3.2}$$

where

ρ = density

μ = dynamic viscosity

U_i = mean-velocity components

p = pressure

u_i' = fluctuating velocity component.

$\overline{u_i' u_j'}$ = Reynolds stresses

The "bar" in equation 3.2 denotes the average value and the subscripts i and j denote the three instantaneous velocity components in the three flow directions. These equations can be used with approximations based on knowledge of the properties of flow turbulence to give approximate averaged solutions.

Averaging Navier-Stokes equations results in six additional unknowns which are referred to as Reynolds stresses, in addition to three original velocity and pressure components. Consequently, the number of the unknowns exceeds the number of equations. Therefore, solving these averaged equations can only be possible by adding additional equations. This exercise is termed as "*closure problem*". The

turbulent stresses $\overline{u_i' u_j'}$ are assumed to act like viscous stresses that are proportional to the mean velocity gradient. This assumption is made by Boussinesq who introduced "turbulent" or "eddy" viscosity concept in 1877. This concept assumes that the turbulent (Reynolds) stresses are proportional to the mean velocity gradients and can be expressed as follows:

$$-\overline{u_i' u_j'} = \nu_t \left(\frac{\partial U_i}{\partial x_j} + \frac{\partial U_j}{\partial x_i} \right) - \frac{2}{3} \left(k + \nu_t \frac{\partial U_i}{\partial x_i} \right) \delta_{ij}, \tag{3.3}$$

where ν_t is the eddy viscosity, and δ_{ij} is the Kronecker delta (which equal 0 if $i \neq j$ and 1 if $i = j$). In contrast to the molecular viscosity ν, the eddy viscosity ν_t is not a fluid property and it depends strongly on the state of the flow. It may vary significantly from one point to another in the flow, and it may vary from flow to another. The eddy viscosity can be modeled as (Pope, 2000)

$$\nu_t = C_\mu f_\mu \frac{k^2}{\varepsilon}, \tag{3.4}$$

or

$$\nu_t = \frac{k}{\omega} \tag{3.5}$$

where C_μ is a constant which depends on the turbulence closure model being used, f_μ is a damping function employed to compensate for Reynolds number effect in the near wall regions, k is the turbulence kinetic energy, ε is the dissipation rate of the turbulence kinetic energy, and ω is the dissipation rate per unit of turbulence kinetic energy. The turbulence terms k, and ε, or ω can be obtained by introducing the transport equation of RANS turbulence closure models.

3.3 RANS Turbulence Closure Models

A turbulence closure model is prescribed by a set of equations (algebraic or differential) which determine the transport terms ($\overline{u_i' u_j'}$) in the mean flow equations and thus close the system of equations. They are based on hypothesis about turbulent processes and they require empirical input in the form of constants or functions. They do not simulate the details of the turbulent motion but only the effect of turbulence on the mean-flow behavior (Pope, 2000). Turbulent transport processes are strongly problem-dependent. For example, they depend on geometrical conditions (wall shape or roughness), on viscous and swirl effects, and buoyancy. Therefore, turbulence models can only give approximate description and are only valid for a certain flow with a particular set of empirical constants (Pope, 2000).

One way of classifying turbulence models would be according to whether (or not) the models use the eddy viscosity concept. Turbulence models can be classified into (Pope, 2000): (i) Eddy viscosity models, (ii) Reynolds stress models and, (iii) Large-Eddy Simulation (LES) models. Experience has shown that the turbulence models can be classified according to the number of transport equation used for the turbulence quantities. They are zero, one-, and two-equation models. The zero-equation model is widely used in practical engineering CFD codes (Pope, 2000). The one-equation model is widely employed in early stages of turbulence modeling and it still in use but for limited flow regions such as the near-wall sublayer where this model is much simpler to use than the other complicated models (Pope, 2000). The two-equation model is employed when additional details of turbulence quantities are required (Pope, 2000). Only two equation eddy-viscosity turbulence models were tested in the present thesis.

3.4 Two-Equation Turbulence Closure Models

In the one-equation models it is difficult to specify empirically the length scale L_i in the case of more complex flows (Pope, 2000). In attempt to eliminate the need for specifying L_i as a function of position throughout the flow, the two-equation models are developed (Pope, 2000). The length scale L_i characterizing the large eddies contains much of the turbulence energy that is subjected to transport processes in a manner similar to the energy k. Two important processes that influence this length scale are the dissipation, which destroys the small eddies and thus effectively increase the eddy size; and vortex shedding connected with the energy cascade, which reduces the eddy size (Pope, 2000). The balance between these processes can be expressed by using transport equation for L_i to find its distribution throughout the flow (Pope, 2000). The L_i transport equation must be solved alongside a transport equation for the velocity scale V, i.e. k-equation. The length scale equations are a combination in the form (Kantha 2004)

$$Z = k^m L_i^n \tag{3.6}$$

The most common combinations which have been proposed are

Dissipation rate (Harlow and Nakayama, 1967) $\varepsilon \propto \frac{k^{3/2}}{L}$

Frequency (Kolmogorov, 1942) $\omega \equiv \frac{k^{1/2}}{L}$

Turbulence vorticity (Spalding, 1972) $\overline{\omega} \equiv \frac{k}{L^2}$

Rotta (1951) kL

The transport equations for some of the above quantities can be obtained by manipulating Navier-Stokes equations with additional assumptions associated with each model. The general transport equation for all variables can be written as following (Mathieu and Scott, 2000)

$$\frac{\partial Z}{\partial t} + U_i \frac{\partial Z}{\partial x_i} = \frac{\partial}{\partial x_i}\left(\frac{\sqrt{k}L}{\sigma_z}\frac{\partial Z}{\partial x_i}\right) + c_{z1}\frac{Z}{k}P - c_{z2}Z\frac{\sqrt{k}}{L_i} + S, \tag{3.7}$$

where σ_z, c_{z1}, and c_{z2} are empirical constants, P is the production of kinetic energy, and S is the secondary source term which depends on the choice of Z. The different two-equation models are, Standard $k-\varepsilon$ model, Low-Reynolds number $k-\varepsilon$ model, Low-Reynolds number $k-\omega$ model, $k-\omega$ Baseline (BSL) model, and $k-\omega$ Shear stress transport (SST) model.

The two models used in this study are briefly described below

a. Two-Equation Standard k-ε Model

The transport equations for the turbulent quantities for k-ε two-equation model of Jones and Launder (1972) are

$$\frac{D\rho k}{Dt} = \frac{\partial}{\partial x_j}\left[\left(\mu + \frac{\mu_t}{\sigma_k}\right)\frac{\partial k}{\partial x_j}\right] + \mu_t \frac{\partial U_i}{\partial x_j}\left(\frac{\partial U_i}{\partial x_j} + \frac{\partial U_j}{\partial x_i}\right) - 2\mu\left(\frac{\partial k^{1/2}}{\partial x_j}\right)^2 - \rho\varepsilon \tag{3.8}$$

$$\left.\begin{aligned}\frac{D\rho\varepsilon}{Dt} = \frac{\partial}{\partial x_j}\left[\left(\mu + \frac{\mu_t}{\sigma_\varepsilon}\right)\frac{\partial \varepsilon}{\partial x_j}\right] + f_1 C_{\varepsilon 1}\mu_t \frac{\varepsilon}{k}\frac{\partial U_i}{\partial x_j}\left(\frac{\partial U_i}{\partial x_j} + \frac{\partial U_j}{\partial x_i}\right)\\ - C_{\varepsilon 2} f_2 \rho\frac{\varepsilon^2}{k} + \rho E\end{aligned}\right\} \tag{3.9}$$

and the eddy viscosity is defined as

$$\nu_t = C_\mu f_\mu \frac{k^2}{\varepsilon} \tag{3.10}$$

where the model constants are given as

$$\left.\begin{aligned} C_\mu = 0.09 \quad \sigma_k = 1.0 \quad \sigma_\varepsilon = 1.3 \\ C_{\varepsilon 1} = 1.44 \quad C_{\varepsilon 2} = 1.92 \end{aligned}\right\} \tag{3.11}$$

with the damping functions as

$$\left.\begin{aligned} f_\mu = f_1 = f_2 = 1 \\ E = 0 \end{aligned}\right\} \tag{3.12}$$

b. Two-Equation k-ω Shear Stress Transport (SST) Model

Following the k-ω model proposed by Wilcox (1988), which has the disadvantage of being highly sensitive to ω in the freestream region, Menter (1994) proposed an improved version of k-ω, which is called shear stress transport (SST) model. The SST model is a combination of the k-ω model of Wilcox (1988), which is recommended to solve for flow in the inner region of the boundary layer, and the standard k-ε for the outer boundary region, as well as the freestream region. The k-ε model is then transformed into k-ω formulation along with the introduction of the blending function F_1. This function is given a value equal to 1 near the wall and zero far from the wall. The difference between the SST model and k-ω model is the appearance of a cross-diffusion term in the ω equation and also the constants are different. The transport equations for the SST model of Menter (1994) are

$$\frac{D\rho k}{Dt} = \mu_t \frac{\partial U_i}{\partial x_j}\left(\frac{\partial U_i}{\partial x_j} + \frac{\partial U_j}{\partial x_i}\right) + \frac{\partial}{\partial x_j}\left[\left(\mu + \sigma_k \mu_t\right)\frac{\partial k}{\partial x_j}\right] - \beta^* \rho \omega k \tag{3.13}$$

$$\frac{D\rho\omega}{Dt} = \frac{\gamma}{\rho}\frac{\partial U_i}{\partial x_j}\left(\frac{\partial U_i}{\partial x_j} + \frac{\partial U_j}{\partial x_i}\right) + \frac{\partial}{\partial x_j}\left[(\mu + \sigma_\omega \mu_t)\frac{\partial \omega}{\partial x_j}\right] \Bigg\} - \beta\rho\omega^2 + 2\rho(1 - F_1)\frac{\sigma_{\omega 2}}{\omega}\frac{\partial k}{\partial x_j}\frac{\partial \omega}{\partial x_j} \Bigg\} \tag{3.14}$$

The constants for the outer region are:

$$\left.\begin{array}{lll} \sigma_{k2} = 0.5 & \sigma_{\omega 2} = 0.5 & \beta_2 = 0.0750 \\ \beta^* = 0.09 & \kappa = 0.41 & \gamma_{21} = \beta_2/\beta^* - \sigma_{\omega 2}\kappa^2/\sqrt{\beta^*} \end{array}\right\} \tag{3.15}$$

The constant for the inner region are

$$\left.\begin{array}{llll} \sigma_{k1} = 0.85 & \sigma_{\omega 1} = 0.5 & \beta_1 = 0.0750 & a_1 = 0.31 \\ \beta^* = 0.09 & \kappa = 0.41 & \gamma_1 = \beta_1/\beta^* - \sigma_{\omega 2}\kappa^2/\sqrt{\beta^*} & \end{array}\right\} \tag{3.16}$$

and the eddy viscosity is now defined as

$$\nu_t = \frac{a_1 k}{\max(a_1\omega; \Omega F_2)} \tag{3.17}$$

where Ω is the absolute value of vorticity, which is defined as

$$\Omega = \frac{\partial U_2}{\partial x_1} - \frac{\partial U_1}{\partial x_2} \tag{3.18}$$

and F_2 is given by

$$F_2 = \tanh(\arg_2^2), \tag{3.19}$$

with

$$\arg_2 = \max\left(2\frac{\sqrt{k}}{0.09\omega y}; \frac{500\nu}{y^2\omega}\right). \tag{3.20}$$

The constants for the model employed for the inner region of the boundary layer, i.e. in the vicinity of the wall, denoted by a symbol φ_1, and the conditions for the model used to solve for the outer region of the boundary layer as well as the

freestream region, denoted by φ_2, are related together by a function called "blending function F_1". The latter provides the constants, φ, for the BSL model as

$$\varphi = F_1\varphi_1 + (1 - F_1)\varphi_2 \tag{3.21}$$

where

$$F_1 = \tanh\left(\arg_1^4\right) \tag{3.22}$$

and

$$\arg_1 = \min\left[\max\left(\frac{\sqrt{k}}{0.09\omega y}; \frac{500\nu}{y^2\omega}\right); \frac{4\rho\sigma_{\omega 2}k}{CD_{k\omega}y^2}\right] \tag{3.23}$$

The symbol y is the distance to the wall and $CD_{k\omega}$ is the positive portion of the cross-diffusion term in the ω-equation, which is given as

$$CD_{k\omega} = \max\left[2\rho\frac{\sigma_{\omega 2}}{\omega}\frac{\partial k}{\partial x_j}\frac{\partial \omega}{\partial x_j}; 10^{-20}\right] \tag{3.24}$$

Freestream Conditions and Wall Boundaries

The freestream mean velocity components, pressure, and turbulence quantities at the inlet of the computational domain are taken as $u = U_\infty$, $v = 0$, $w = 0$, $p = p_\infty$, $k = k_\infty$ and $\omega = \omega_\infty$. The freestream k_∞, ε_∞ and ω_∞ are estimated by using the following relations (Menter, 1994; Karel, 1998): $k_\infty = 1.5\left(I_\infty \times U_\infty\right)^2$, $\varepsilon_\infty = c_\mu f_\mu \rho \mathrm{Re} k_\infty^2 / \mu_{t\infty}$ and $\omega_\infty = \rho_\infty\left(k_\infty/\mu_\infty\right)\left(\mu_{t\infty}/\mu_\infty\right)^{-1}$ where $\mu_{t\infty}$ is the freestream turbulent viscosity which is approximated as $\mu_{t\infty} \sim (0.1 - 10)\mu_\infty$. The existence of a solid boundary (wall) induces considerable changes in the flow and

turbulence structure as compared to the turbulent freestream away from the wall. Therefore, the flow conditions at the wall must be defined. The no-slip boundary conditions are used for velocities, however, zero gradients are used for pressure as follows $U_w = V_w = W_w = 0$ and $\partial p_w / \partial n = 0$ where n is the normal direction onto the wall. For turbulence quantities, i.e., kinetic energy k, viscosity μ_t, dissipation ε, specific dissipation ω, and their values at the wall are set as $k_w = 0$, $\mu_{t,w} = 0$, $\varepsilon_w = 0$, and $\omega_w = 800\mu_w / \rho_w (\Delta y_1)^2$ where Δy_1 is the distance to the next node away from the wall (Kral 1998, Menter 1994).

Chapter 4

SOLUTION ALGORITHM

In the present thesis, two different numerical approaches are used. One is a Cartesian based-grid blocked-off technique, and the other is the conventional technique implemented in Fluent software. The former is a new method developed by Birouk and Abou Al-Sood (2007) to solve for the flow characteristics around a spherical object, for which details are provided below. However, the latter is a conventional method employed by the commercial software Fluent, which is different than the former one.

4.1. Cartesian-Grid Based Blocked-off Technique

The grid generation, treatment of the sphere in the calculation domain, and independency of the results on the grid are discussed below.

4.1.1 Numerical approach.

Finite-volume approach (Patankar 1980) with staggered grid is used to solve the complex nonlinear and strongly coupled set of governing transport equations described in chapter 3. The governing differential equations are integrated over discrete volumes in Cartesian coordinates resulting in a set of algebraic equations of the following general form

$$\left(a_E + a_W + a_N + a_S + a_T\Phi_T + a_B - S_P\Delta x\Delta y\Delta z\right)\Phi_P = a_E\Phi_E + a_W\Phi_W + a_N\Phi_N + a_S\Phi_S + a_T\Phi_T + a_B\phi_B + S_C\Delta x\Delta y\Delta z \quad (4.1)$$

where a_P, a_E, a_W, a_N, a_S, a_T, a_B, and b_Φ are coefficients and their expressions are reported elsewhere (Aboul Al-Sood, 2007; Birouk and Abou al-Sood, 2007). S_P and S_C are the two terms of linearized source term S_Φ, and Δx, Δy, and Δz are the control volume lengths in the direction of x, y, and z coordinates respectively. A schematic of the CVs is presented in Figure 4.1.

The absence of an explicit equation for pressure when working numerically with the so-called primitive variables U, V, W and p, presents a real difficulty which is overcome by using the SIMPLEC approach (Van Doormall and Raithby, 1984). This approach allows developing an expression in the form of Eq. (4.1) for the pressure through a combination of the continuity and momentum equations. The objective is to develop a pressure field such that the resulting velocity field satisfies the continuity equation for every control volume in the calculation domain. The solution of the set of linearized algebraic equations, which are resulted from the application of Eq. (4.1) to each control volume in the computational domain, is accomplished by using a three-dimensional Strongly Implicit Procedure (SIP) developed by Leister and Perić (1991). The SIP is chosen as a solver because it takes less number of iterations for convergence compared to other solvers, such as point Successive Over Relaxation (SOR) or Line Successive Over Relaxation (LSOR). Details of SIP, SOR and LSOR are reported elsewhere (Abou Al-Sood, 2006). The iterative procedure sweeps the solution domain until either the assigned maximum number of iterations is exceeded or the range-normalized relative errors

(Eq. 4.2) of the diffusion parameters (U, V, W, p, k, and ε or ω) are satisfied for each control volume.

$$\left| \frac{\Phi^{n+1} - \Phi^{n}}{\Phi_{\max} - \Phi_{\min}} \right| \leq \Theta_{\Phi}, \tag{4.2}$$

where Φ^{n+1} and Φ^{n} are the new and previous values of the diffusion parameter Φ. Φ_{max} and Φ_{min} are the maximum and minimum value for the entire Φ^{n+1} field and Θ_{Φ} is taken to be 10^{-4} for all quantities.

4.1.2 Treatment of a Sphere in the Calculation Domain.

The sphere is treated, in the computational domain, by employing the blocked-off treatment. This treatment is achieved by blocking-off the control volumes (CVs) that form the sphere (i.e. the inactive CVs) so that the remaining active control volumes form the desired domain (i.e., the surrounding gaseous phase). It is obvious that the sphere is approximated by a series of rectangular or/and square CVs. Although the computation is executed for the entire domain, only the solution within the active control volumes is meaningful. The simplest way in which the desired values of these parameters could be obtained in the inactive control volumes (i.e. sphere) is by assigning a large source term in the discritized equation. That is setting S_C and S_P in Eq. (4.1) for the inactive zone as follows:

$$S_C = 10^{30}\Phi_{P,desired} \qquad \text{and} \qquad S_P = -10^{30} \tag{4.3}$$

where 10^{30} is a number large enough so that the other terms in the discritized equation become negligible. Therefore, Eq. (4.1) for the sphere (inactive CVs) becomes

$$S_C + S_P \Phi_P = 0 \tag{4.4}$$

and hence

$$\Phi_P = -S_C / S_P = \Phi_{P,desired} \,. \tag{4.5}$$

In case of a solid stationary sphere, the desired values ($\Phi_{P,desired}$) for all parameters (i.e. pressure, velocity components and turbulence quantities) are set equal to zero. Note that this technique makes the surface of the sphere looks like stair steps as illustrated in Fig. 4.1. This approximation induces some calculation errors which can be minimized by using a very fine grid in the droplet domain.

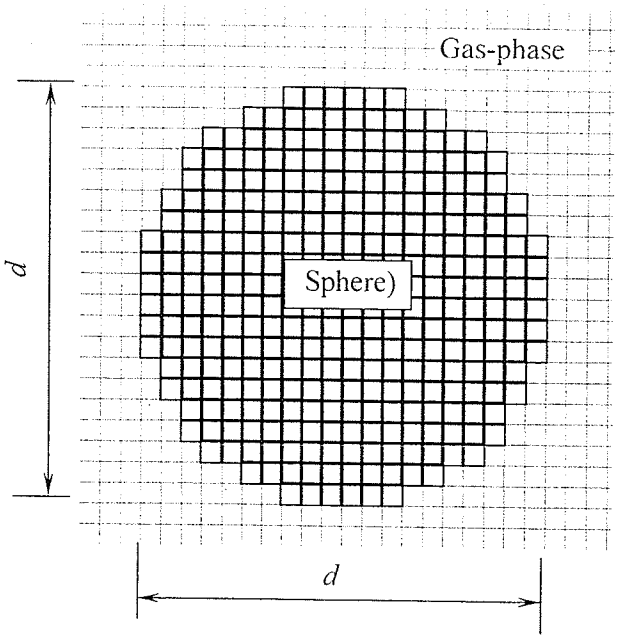

Fig. 4.1 The Cartesian-based blocked-off treatment of a sphere immersed in the computational domain

4.1.3 Grid generation and results independency.

For the Cartesian based blocked-off technique, the calculation domain, which is a cube of $32r$ x $32r$ x $32r$ length, where r is the sphere radius, was divided into several control volumes and the sphere is fixed at the centre of the cube. This choice is based on the suggestions made by Sundararajan and Ayyaswamy (1984) who recommended that the freestream inflow and boundary conditions must be taken at a distance from the centre of the sphere that is at least ten times greater than the sphere radius. The boundary conditions for the computational domain are taken as follows: The left and right faces are considered inflow and outflow boundary conditions, respectively; whereas for the other faces, north, south, top and bottom, are taken as the wall boundary conditions. In the present analysis, the Cartesian grid in the calculation domain consists of 60x60x60. Since the gradients around the sphere are large, a very fine grid 40x40x40 is used in the domain of $4r$, i.e. 2r from the sphere centre in all directions, as shown schematically in Fig. 4.2. This number of grids is found to be the optimum number that provides stable results with an acceptable computational time. Coarser grids, such as 40x40x40 for the entire calculation domain and 30x30x30 for the domain of $4r$ have also been tested. However, their outcome showed, for example, that the laminar drag coefficient, at a typical Reynolds number Re =100 is lower than its experimental counterpart by about 20%. To eliminate the dependence of the results on the grid, other very fine grids have also been tested such as, for example, 80x80x80 for the entire computation domain and 50x50x50 for the $4r$ domain but the computational time is extremely long. This exercise is continued until the grid dependency is practically eliminated. A summary of the sensitivity of the present model predictions on the chosen grid is given in Table 1. Finally, it is important to point out that Fig. 4.2

does not show the complete computational grid but only an illustration to provide a general idea. On the other hand, this figure shows that the uniform grid is fine in the *4r* region, which is twice the size of the sphere, and coarse outside of this region.

Table 4.1
Grid independency for the blocked-off technique

	Domain	Grid		
	32r₀ (see Fig. 4.2)	40×40×40	60×60×60	80×80×80
	4r (see Fig. 4.2)	30×30×30	40×40×40	50×50×50
C_D	Laminar flow (Re=100)	1.3547 (19.23%)	1.1384 (-----)*	1.1099 (2.50%)
	Turbulent flow (*k*-ε model) (Re=100, I_∞=20%)	1.4912 (24.20%)	1.2006 (-----)	1.2731 (6.04%)
	Turbulent flow (SST model) (Re=100, I_∞=20%)	2.1147 (82.09%)	1.1614 (-----)	1.1882 (2.31%)

* The error is based on the optimum grid 60×60×60 in the whole domain with 40×40×40 in the *4r* domain

4.2. Conventional Technique

The set of equations describing the flow over sphere with the boundary conditions reported previously in Chapter 3 are solved numerically using Fluent 6.1.22 which is based on finite volume formulation. The computational domain was subdivided into a number of small control volumes by creating a computational grid that consists of tetrahedral-shaped cells. The details of grid generation and the numerical approach are provided below.

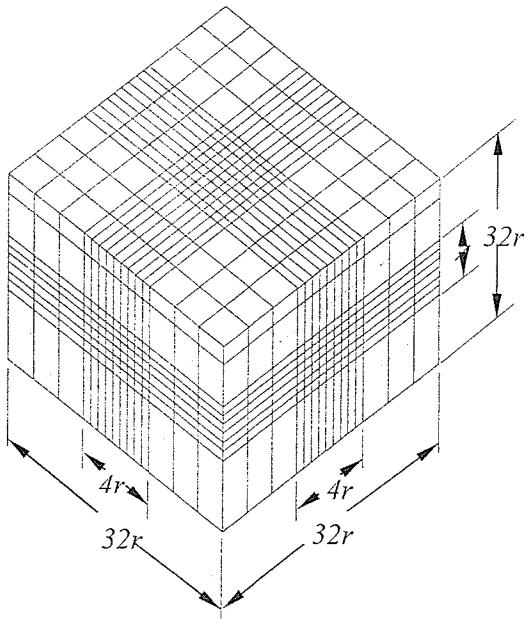

Fig. 4.2 Schematic of the computational Cartesian grid

4.2.1 Grid Generation and Results Independency

Gambit was used to generate the computational grid for the domain around the sphere. The sphere was fixed in the center of a 12 mm radius spherical domain. The spherical domain, which has a radius of 12 mm, was then divided into two domains. The first domain, which surrounds the sphere, (referred to in this chapter as the inner domain) extends from r = 1 mm to 3 mm. The outer domain, which is referred to in this chapter as the outer domain, extends from r = 3 mm to 12 mm. The choice of a computational domain with a radius of 12 mm is based on the recommendation of Sundararajan and Ayyaswamy (1984), who suggested that the freestream inflow and boundary conditions must be taken at a distance from the center of the sphere

that is at least ten times greater than the sphere radius. Both inner and outer spherical domains were then subdivided into a number of small control volumes of tetrahedral-shaped type. In order to have a very fine grid in the immediate surrounding of the sphere, the control volumes of the inner domain were chosen to be much smaller than those of the outer domain. Spacings of 0.06 and 0.5 were used for the inner and outer domain, respectively, which resulted in a domain of 2,555,146 tetrahedral cells. This grid was found to be the optimum that provides stable results with an acceptable computational time. Figure 4.4 shows a cross-section of the computational domain. The grid independency was successfully achieved when the results of the last grid agreed fairly well with those obtained by the coarser grid that has spacings of 0.08 and 0.6 for both inner and outer domains, respectively. Also, much coarser grid with spacings of 0.15 for the inner domain and 0.8 for the outer domain is tested and the difference in the results between this grid and the finest grid is noticeable. For example, at Re = 200 (laminar flow) the predicted drag coefficient is found to be higher that that obtained by the finest grid by approximately 8%. A typical assessment of the sensitivity of the model predictions to the chosen grid is shown in Table 4.2 for a typical Reynolds number Re = 100 and a turbulence intensity I = 30%. The error is based on the predictions of the optimum (fine) grid. More information about grid-independency is provided in the next chapter.

Table 4.2
Sensitivity of present model predictions to the chosen grid (the error is calculated with respect to the fine grid predictions)

	Domain	Coarse Grid	Medium Grid	Fine Grid
	12r	0.8	0.6	0.5
	3r	0.15	0.08	0.06
C_D	Laminar flow (Re = 100)	1.22174 (9.92%)	1.13164 (1.8%)	1.1105967 (-----)
	Turbulent flow ($k-\varepsilon$ model) (Re = 100, I = 30%)	1.423017 (15.13%)	1.26787 (2.51%)	1.236107 (-----)
	Turbulent flow (SST model) (Re = 100, I = 30%)	1.34317 (17.54%)	1.17401 (2.44%)	1.14612 (-----)

* The Reynolds number is based on the sphere diameter and the air-freestream mean-velocity upstream the sphere. The relative intensity of the turbulence is defined as $I_\infty = u' / U_\infty$.

4.2.2 Numerical Approach

The commercial software, Fluent version 6.1.22, which is based on finite volume formulation is employed to solve the governing equations described in chapter 3. Details about the solution algorithm are provided in appendix A.

The simulation was carried out using QUICK (Quadratic Upwind Interpolation) for momentum, turbulence kinetic energy, and turbulence dissipation rate. PRESTO (PRESsure STaggering Option) was used for pressure interpolation. PISO (Pressure-Implicit with Splitting of Operators) was used for Pressure-Velocity Coupling. The solution convergence is assumed when all of the residuals parameters fall below 0.5×10^{-05}.

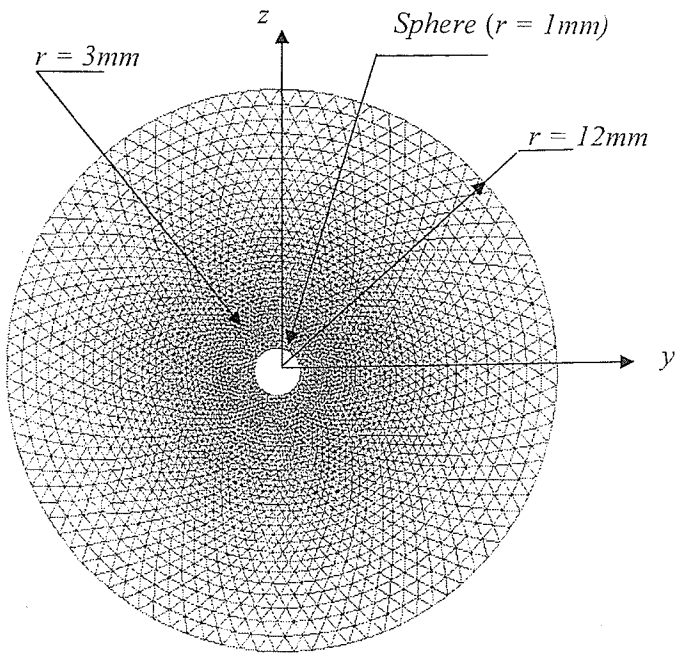

Figure 4.4 A cross-section of the computational domain in the *y-z* plane

Chapter 5

RESULTS AND DISCUSIONS

The main results presented in this chapter concern the numerical predictions of the mean drag coefficient of a sphere exposed to a turbulent airstream. The ultimate objective is to assess the level of accuracy of the predictions of the Cartesian grid-based blocked-off technique (termed hereafter as the new method) by comparing its predictions with their counterparts' obtained by using a conventional method implemented in the CFD software Fluent (referred hereafter as the conventional method). Comparisons include, in addition to the sphere drag coefficient, the local pressure and shear stress (i.e. skin friction) coefficients. Note that the calculation of the sphere mean drag coefficient is simply the summation of the integrals of the wall pressure and shear stress coefficients over the surface area of the sphere, which is expressed as

$$C_D = \int_0^{\pi} C_p \sin(2\phi) d\phi + \frac{1}{\rho U_\infty^2} \int_0^{\pi} \tau_w (1 - \cos(2\phi)) d\phi \qquad (5.1)$$

= pressure drag coefficient + viscous drag coefficient

where

ϕ = The azimuthal angle

C_p = The wall pressure coefficient = $\dfrac{p - p_\infty}{\frac{1}{2}\rho U_\infty^2}$

τ_w = The shear stress = $\mu\left(\frac{\partial U_i}{\partial x_j}+\frac{\partial U_j}{\partial x_i}\right)+\frac{2}{3}\left(\frac{\partial u_j}{\partial x_j}\right)\delta_{ij}$

It is important to mention here that all the predictions presented below are obtained with the corresponding optimum grid (referred to here as fine grid) for each method (the predictions are no longer grid dependent or the variation of the predictions is insignificant).

5.1 Laminar Flow Results

The computational results of the sphere drag coefficient obtained by using a fine, medium, and a coarse grid and presented in Figure 5.1 over wide range of Reynolds numbers. Figure 5.2 displays a comparison of the local wall pressure coefficient as predicted by the new method (i.e. blocked-off technique) and Fluent, as well as with published data (Kim *et al.,* 2001). It is important to point out that all the three predictions are produced by three different numerical methods. The comparison made in Fig. 5.2, which is for a typical Reynolds number of 100, shows only unnoticeable difference between the present predictions (both methods) and published data of Kim (2001). There is only a slight difference which is can be seen between two azimuthal positions along the periphery of the sphere, i.e. between 30° and 70° and, between 100° and 150°, respectively. Within these regions the maximum difference between the present predictions and published data quoted in Fig. 5.2 is less than around 10% which can be due to computational error. Nevertheless, the comparison made in Fig. 5.2 shows an excellent agreement between the two methods employed in the present study, as well as with the data of Kim *et al.* (2001).

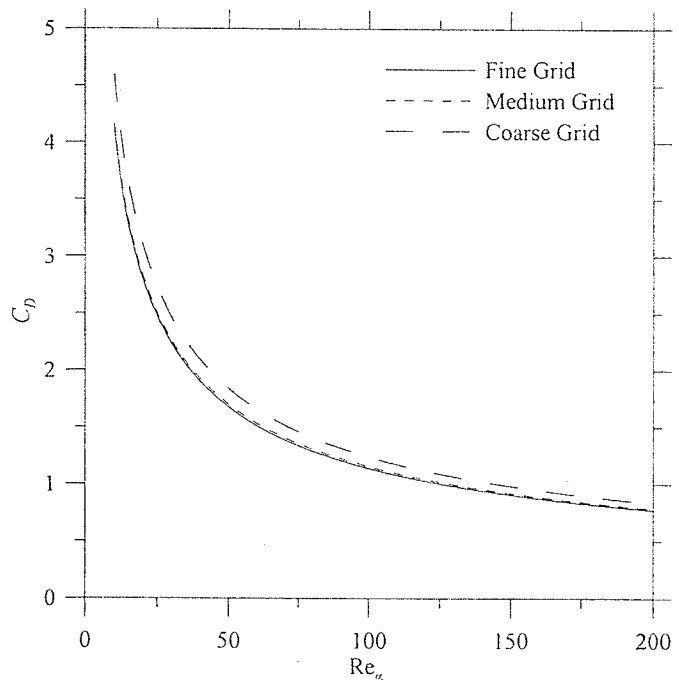

Fig. 5.1 The predicted drag coefficient versus Reynolds number for fine, medium, and coarse grid

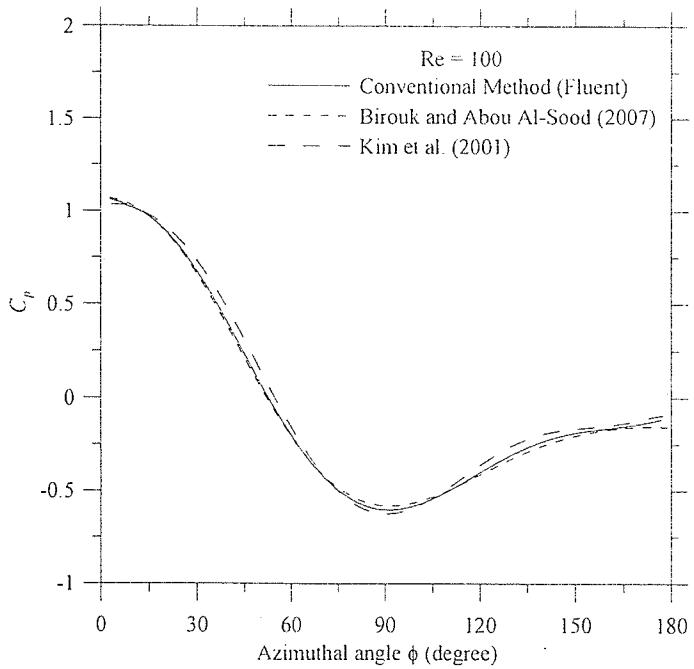

Fig. 5.2 Local wall pressure coefficient versus azimuthal angle for a typical Reynolds number of 100

The predicted sphere mean drag coefficient over a wide range of Reynolds number is reported in Fig. 5.3. Note that the Reynolds number is based on the freestream velocity and sphere diameter. This figure illustrates also a comparison between the two methods employed in the present study as well as against the experimental data of Roos and Willmarth (1977). The comparison made in Fig. 5.3 clearly demonstrates an excellent agreement between the two different numerical methods employed here. It shows also that these numerical predictions agree very well with the experimental data.

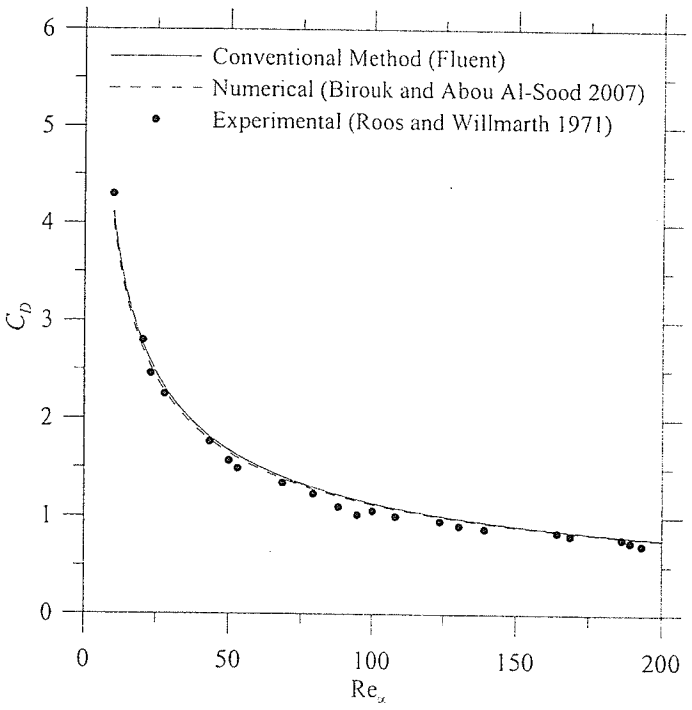

Fig. 5.3 Comparison of the sphere mean drag coefficient between the present predictions (new method and Fluent) and published experimental data

Figure 5.4 shows the variation of the wall pressure coefficient with the azimuthal angle, obtained by Fluent, for different Reynolds numbers that are ranging from 50 to 200. This figure shows that the local wall pressure coefficient is noticeably different for different Reynolds numbers in the range of the azimuthal angle between 50 and 180 degree here it increases with Re. Whereas, for $\phi < 45^0$, the local pressure coefficient decreases slightly with increasing Re.

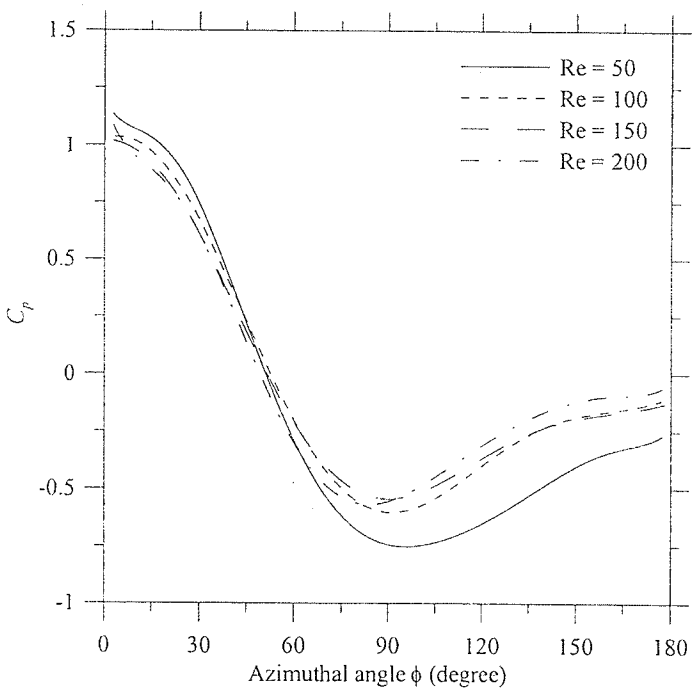

Figure 5.4 The predicted wall pressure coefficient over the sphere for different Reynolds numbers

Figure 5.5 shows the distribution of the sphere surface local skin friction coefficient over a wide of Reynolds numbers (Re = 50, 100, 150, and 200). This figure shows that the local skin friction decreases with increasing Reynolds number in the range when the azimuthal angle is less than approximately 135°. Beyond this angle the local skin friction coefficient is almost vanished due to the separation of the boundary layer, and therefore, this angle is called the separation angle. We can also observe that the local skin friction coefficient reaches its peak when the azimuthal angle is around 60° independently on Re.

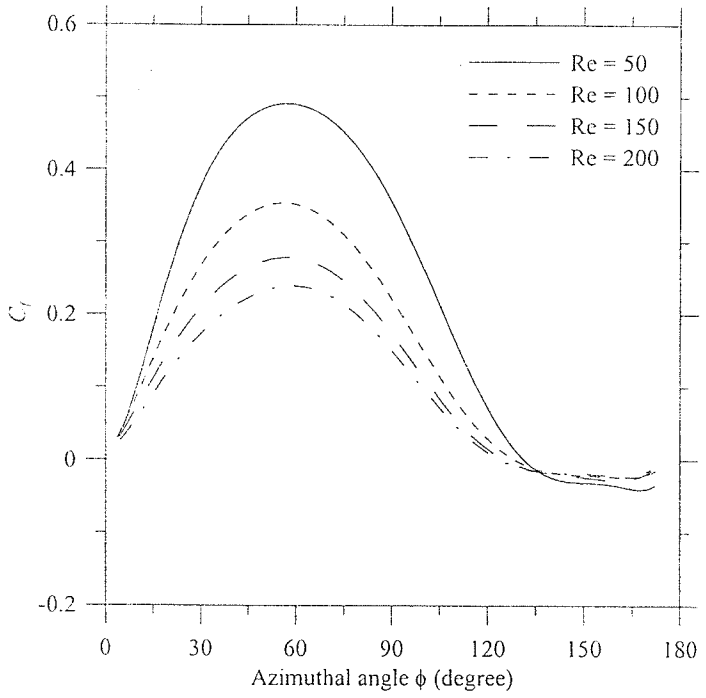

Figure 5.5 The predicted local skin friction coefficient over the sphere for the different Reynolds numbers as predicted by the conventional method

5.2 Turbulent Flow Results

Turbulent flow results of the sphere mean drag coefficient and its components (i.e. local pressure and skin friction coefficients) obtained by the eddy-viscosity turbulence models, the standard k–ε model and k–ω shear stress transport (SST) model are presented below. Three typical Reynolds numbers (10, 50, and 100) are chosen with turbulence intensities ranging between 10 and 60%.

Figures 5.6 and 5.7 present the turbulent (based on k-ε model) local variation of the wall pressure coefficient predicted by using the standard k-e model for a typical turbulence intensity of 30% and two typical Reynolds numbers of 10 and 100, respectively. These figures show that there is a fair agreement between the predictions of the new method and those by Fluent. Only slight differences is found at a Re = 10 where the difference in the predictions between the two methods is less than 9%. Figures 5.8 and 5.9 present a comparison of the local variation of the sphere skin friction coefficient between the prediction of the new method and those by using Fluent. These predictions are obtained by using the standard k-ε model for the same conditions of Figs. 5.6 and 5.7. Similarly to the turbulent local sphere wall pressure coefficient, the comparison between the two methods of the sphere skin friction is very good, especially for Re = 100. Figures 5.10-5.13 present the variation of the local sphere wall pressure and skin friction coefficients, as predicted by using the SST model, for the same flow conditions of Figs. 5.6 – 5.9. These figures reveal that the predictions of the two different methods are overall in reasonable agreement. Based on the observations in Figures 5.6 through 5.13, it can be concluded that the predictions of the new method are reproduced by using a completely different method (Fluent), although slight differences are observed particularly at very low Reynolds number. This is an indication that the Cartesian

grid-based technique (i.e. new method) is deficiency although the exact sphere surface profile is not captured by this methods, as it looks like step stairs. However, the use of extremely fine grid for the calculation domain in the vicinity of the sphere makes it possible to approach the real sphere.

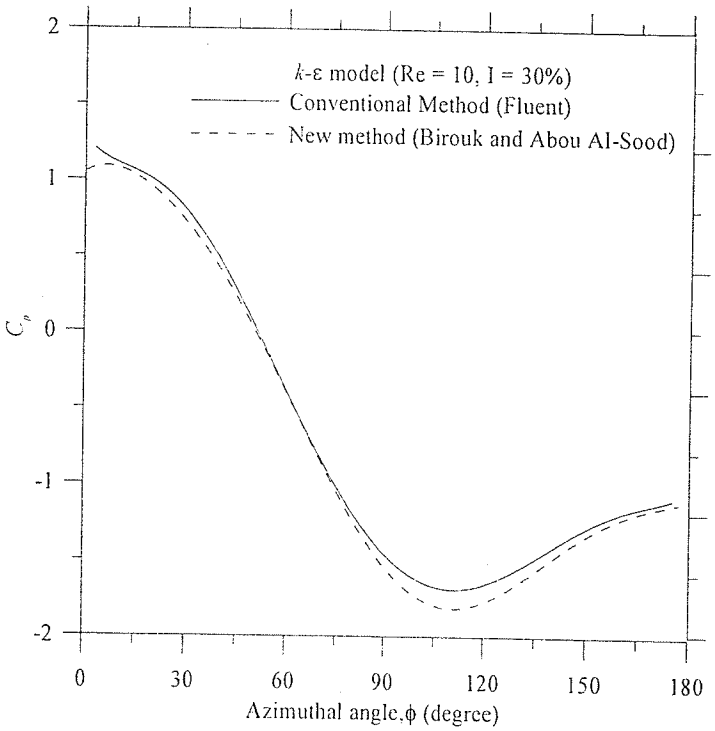

Fig. 5.6 Predictions of the wall pressure coefficient versus azimuthal angle for Re = 10 and I_∞= 30% by using the standard k-ε model

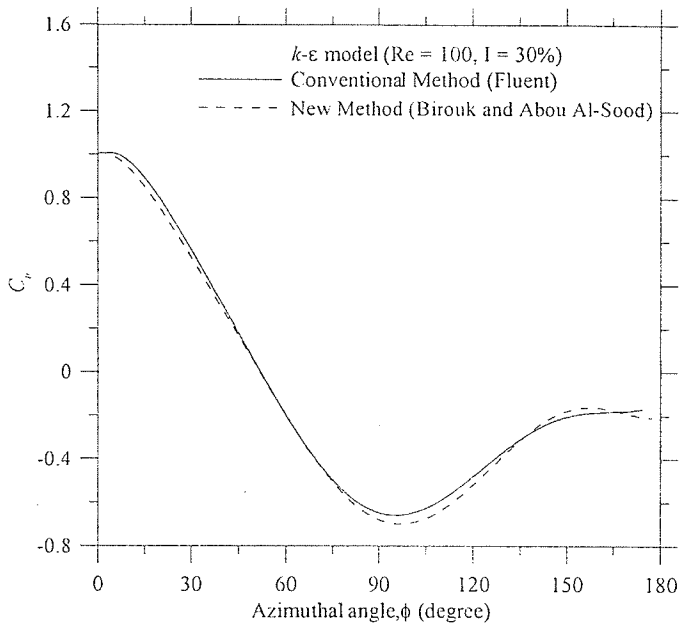

Fig. 5.7 Predictions of the wall pressure coefficient versus azimuthal angle for Re = 100 and I_∞ = 30% by using the standard k-ε model

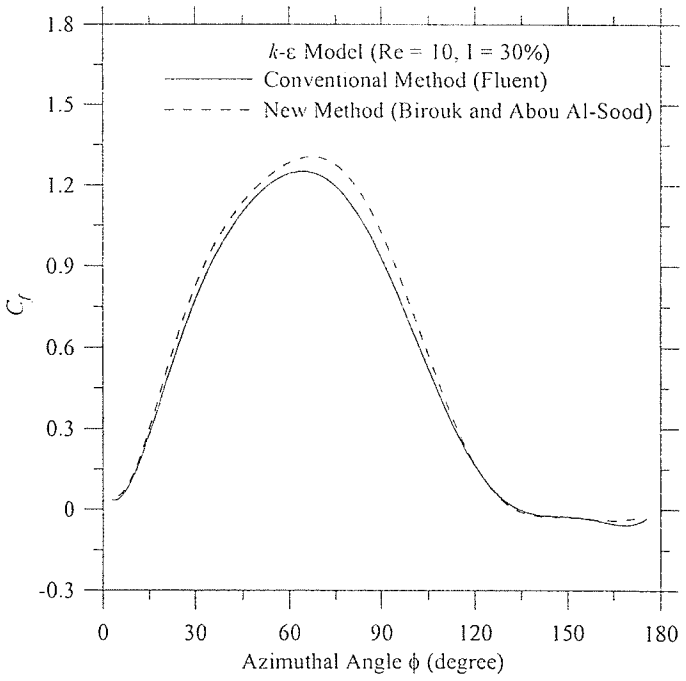

Fig. 5.8 Predictions of the skin friction coefficient versus azimuthal angle for Re = 10 and I_∞ = 30% by using the standard k-ε model

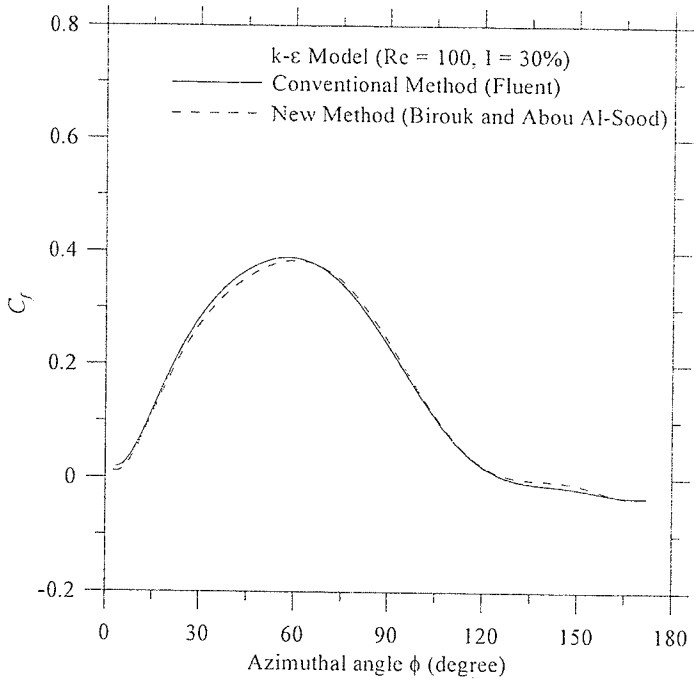

Fig. 5.9 Predictions of the skin friction coefficient versus azimuthal angle for Re = 100 and I_∞= 30% by using the standard k-ε model

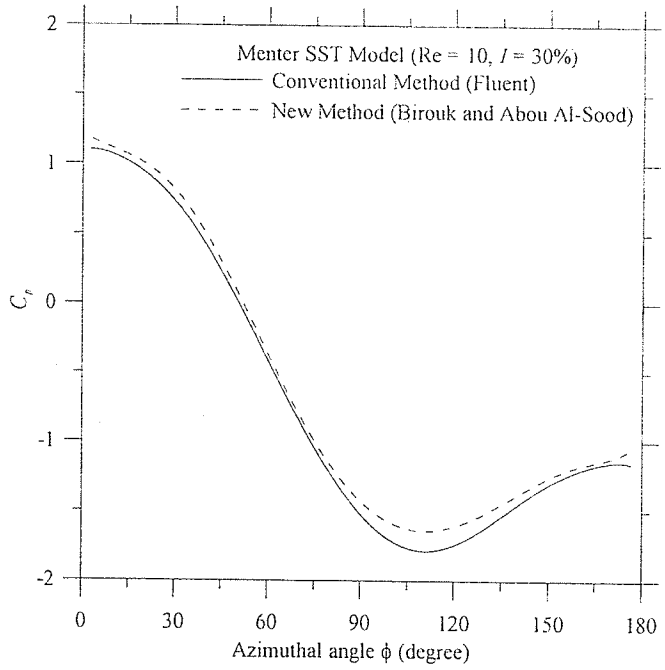

Fig. 5.10 Predictions of the wall pressure coefficient versus azimuthal angle for Re = 10 and I_∞= 30% by using the SST model

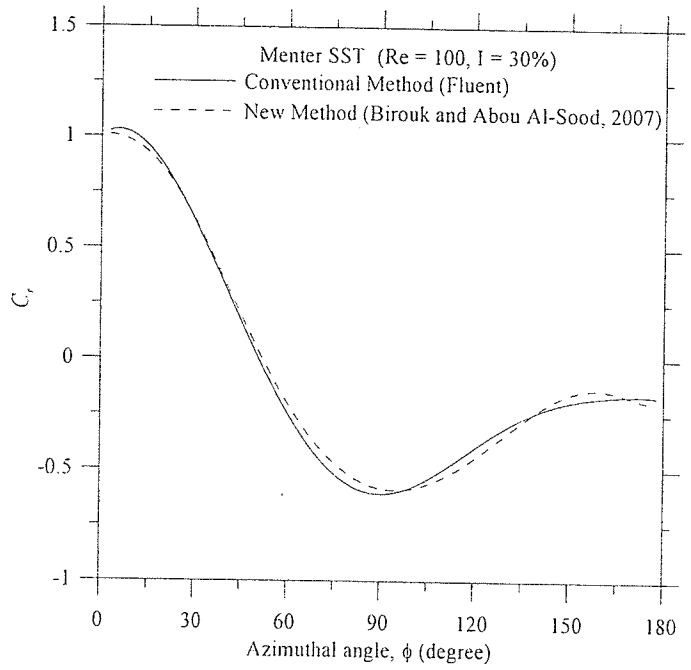

Fig. 5.11 Predictions of the wall pressure coefficient versus azimuthal angle for Re = 100 and I_∞= 30% by using the SST model

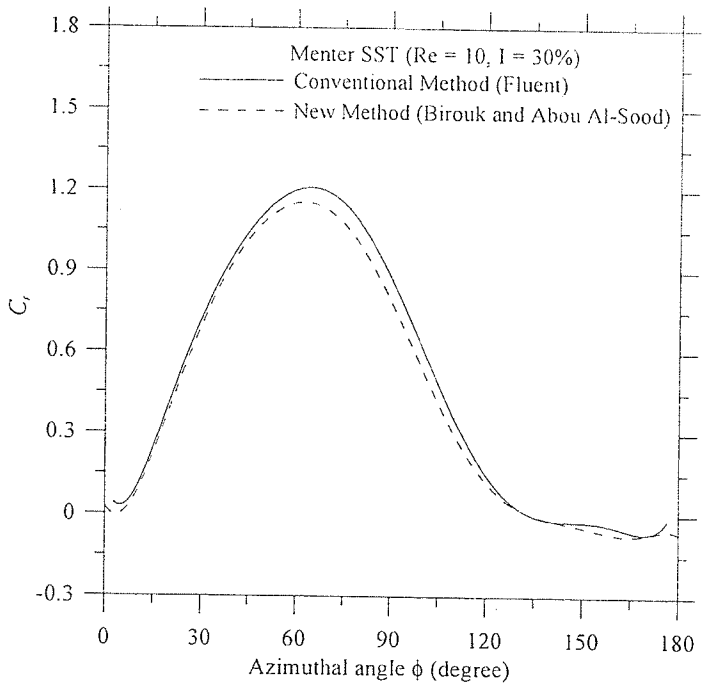

Fig. 5.12 Prediction of the skin friction coefficient versus the azimuthal angle for Re = 10 and I_∞= 30% by using the SST model

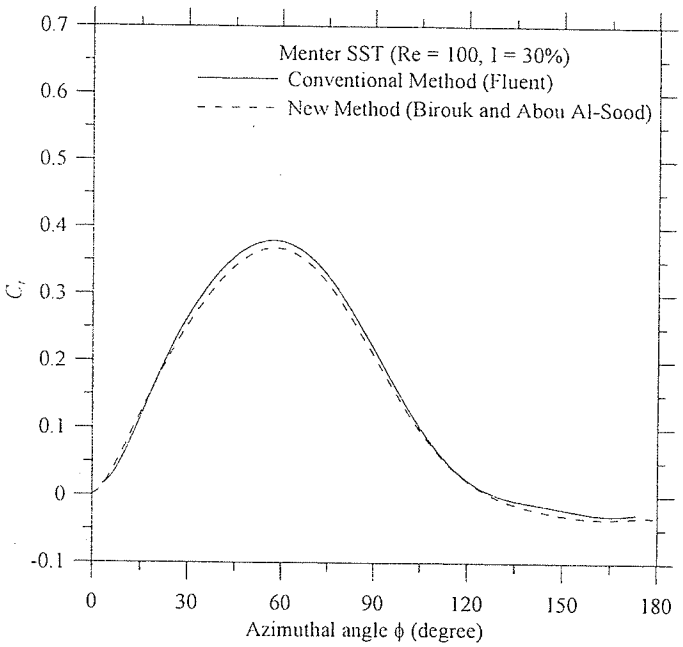

Fig. 5.13 Prediction of the skin friction coefficient versus versus the azimuthal angle for $Re = 100$ and $I_\infty = 30\%$ by using the SST model

Figures 5.14 and 5.15 display the variation of the sphere mean drag coefficient with the airstream turbulence intensity for three typical Reynolds numbers (10, 50 and 100). The predictions of the standard k-ε and SST models are presented in Figs. 5.14 and 5.15, respectively. Both figures reveal that the freestream turbulence intensity does not have an effect on the sphere drag coefficient, as reported in Birouk and Abou Al-Sood (2007) and Abou Al-Sood (2007). These figures show also that the SST model is capable of reproducing similar data to the sphere standard drag coefficient regardless of the magnitude of Reynolds number. Whereas, the standard k-ε model, which is also capable of reproducing the sphere standard drag coefficient at relatively high Reynolds number of approximately 100 or greater, is deficient at relatively lower Reynolds numbers.

It is important to point out here that these conclusions apply to both numerical methods, i.e. the new method and that employed by Fluent. It is, therefore, plausible to conclude that the fact that the standard k-ε model is deficient at low Reynolds numbers is not a consequence of to the new method (i.e. the Cartesian grid-based blocked-off technique) developed for the first time by Birouk and Abou Al-Sood (2007) to study a flow over a spherical object. Although, Figs. 5.14 and 5.15 still show slight discrepancy in the predictions between the two numerical methods (i.e. new method and that employed by Fluent commercial code), these slight discrepancies are not significant and thus cannot be the reason for the deficiency of the k-ε model in reproducing the sphere standard drag coefficient at low Reynolds numbers. The computational results for the drag coefficient for both fine and medium grid are presented in Figure 5.16 and 5.17 for more verification on the accuracy of the grid.

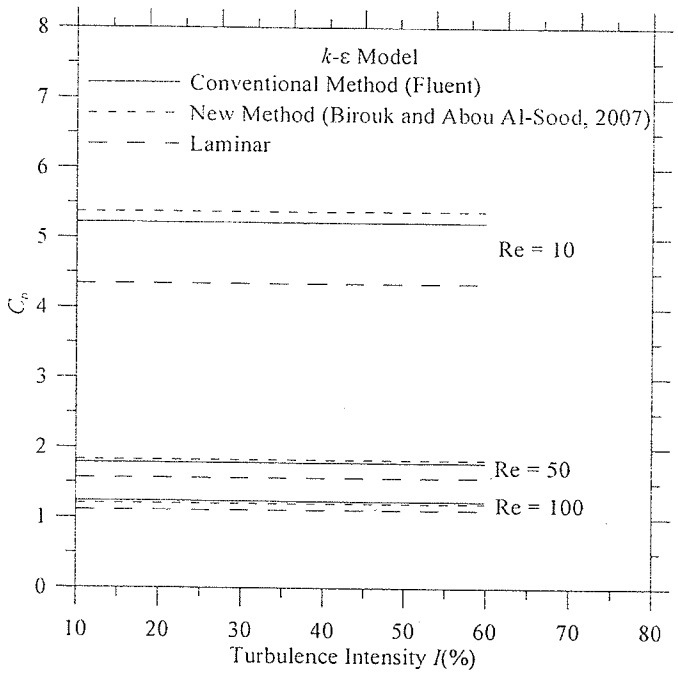

Fig. 5.14 Sphere mean drag coefficient (based on the standard k-ε model) versus the airstream turbulence intensity for different Reynolds numbers

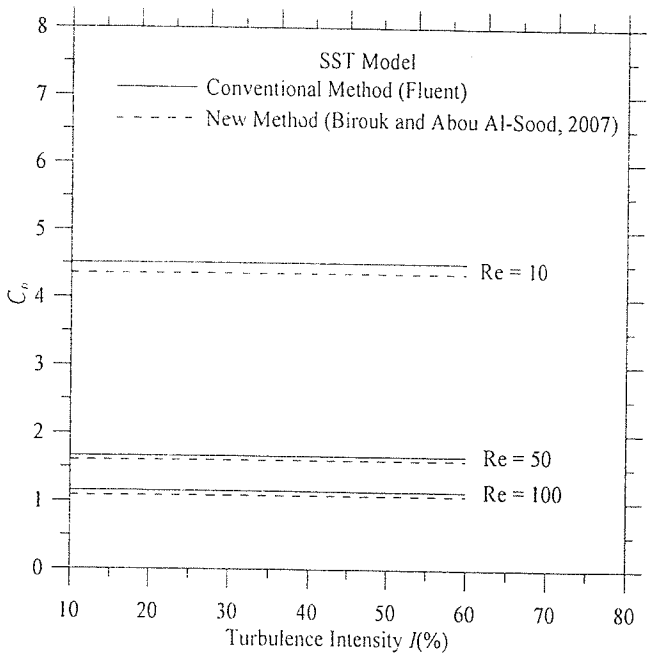

Fig. 5.15 Sphere mean drag coefficient (based on the SST model) versus the airstream turbulence intensity for different Reynolds numbers

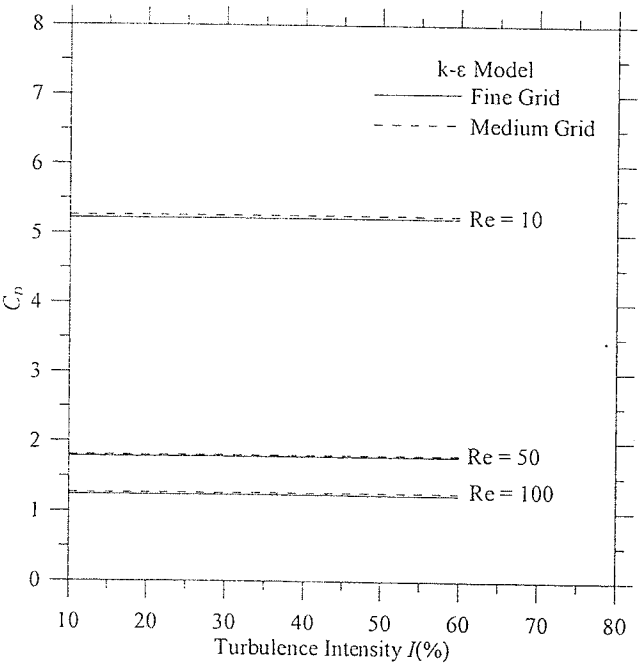

Fig. 5.16 Evaluation of the grid effect on the predicted drag coefficient versus the turbulence intensity at various Reynolds numbers

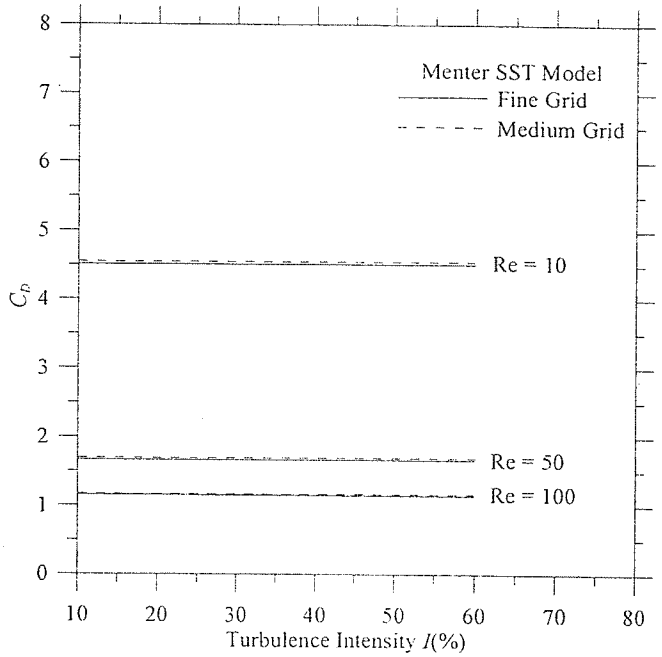

Fig. 5.17 Evaluation of the grid effect on the predicted drag coefficient versus the turbulence intensity at various Reynolds numbers

Chapter 6

CONCLUSIONS

A newly developed numerical method, which is developed for solving laminar/turbulent flow over a sphere has been evaluated. This method is based on solving the mass and momentum conservation equations in Cartesian coordinates by using a blocked-off technique. Although this new numerical method cannot capture the exact/real surface profile of the spherical object, reasonably good predictions for laminar flow are obtained when compared to experiments. For turbulent flow, the predictions of the numerical model are shown to depend much on the turbulence closure model. For example, the SST model is shown to successfully predict correct data while the standard k-ε model fails especially in the low range of Reynolds numbers. An independent method (i.e. a conventional method implemented in Fluent) is employed to verify the degree of the prediction accuracy of the new numerical method. The outcome is that both numerical methods are able to reproduce nearly identical predictions demonstrating the ability of the new technique in generating quality predictions. Finally, it is important to point out that the new numerical method is simple, easy to implement and cost effective in comparison with any published numerical method for studying a flow over sphere.

Appendix A

A SHORT DESCRIPTION OF THE FLUENT SOLVER

This appendix will only discuss the numerical scheme applied in the present calculations by using FLUENT (version 6.1.22). This software has been used in this study to solve the governing equations of the flows described in chapters 3. This code employs finite volume formulation. With the control-volume-based technique used in Fluent, the governing equations are converted into algebraic equations. Subsequently, these produced algebraic equations are solved numerically. About each control volume, the governing equations are integrated in order to produce discrete equations. These discrete equations conserve each quality on a control-volume basis. The description of all options available in Fluent is not the task of this thesis. More information can be found in (Fluent, 2001), however, an overview of the methods used in the present study is provided below.

Segregated Solver

In the present calculations, the governing equations are solved sequentially by using the segregated solution method together with the implicit linearization method. Because the governing equations are non-linear and coupled, several iterations must be performed before a converged solution is obtained. The update is based on the current or the initialized solution depending on the iteration run. The segregated solution method is outlined in the flow chart shown in Figure A.1.

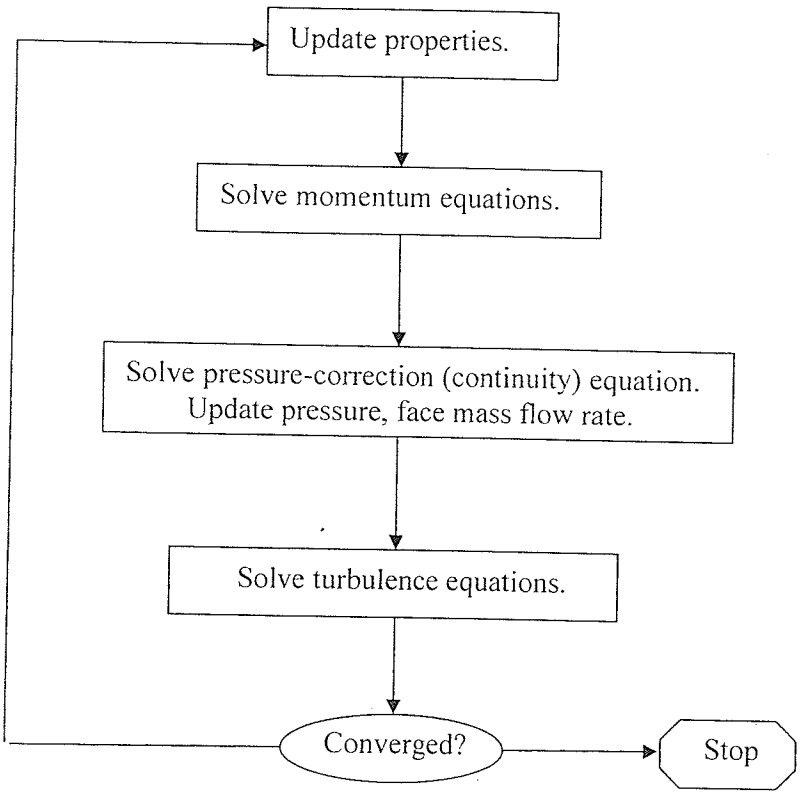

Figure A.1 Overview of the Segregated Solution Method (Fluent, 2001)

Implicit Linearization

Implicit formulation of the linearization means that for the calculation of a given variable both known and unknown values from the neighboring cells are used. This results in each unknown value appearing in more than one equation in the system so that the equations have to be solved simultaneously for all cells to give the unknown values. In other words, all cells are considered at the same time when solving for a single variable field. Then, the next variable field is determined by again considering all cells at the same time. This process continues until updated values for all variables are obtained.

Discretization

Discretization is the process of finding a solution for a general variable ϕ by considering a set of values of the dependent variable at discrete locations instead of its continuous exact solution. For this, the calculation domain is divided into cells (control volumes) which together make up the computational grid. The solution at any one grid point is assumed to be an algebraic function of the solution at its neighboring grid points. Grid points correspond to cell (or face) centers in FLUENT. Discretizing the governing equations can be illustrated, for example, by considering steady-state conservation equation for transport of a scalar quantity ϕ. A written equation in integral form for an arbitrary control volume V is used to demonstrate the discretization as follows:

$$\oint \rho\phi\vec{v} \cdot d\vec{A} = \oint \Gamma_\phi \nabla_\phi \cdot d\vec{A} + \int_V S_\phi dV \qquad \text{(A.1)}$$

where

ρ = density

$\vec{v}$ = velocity vector

$\vec{A}$ = surface area vector

Γ_ϕ = diffusion coefficient for ϕ

∇_ϕ = gradient of ϕ

S_ϕ = source of ϕ per unit volume

Equation A.2 is applied to each control volume in the computational domain and its discretization on a given cell yields:

$$\sum_{f}^{N_{faces}} \rho_f \vec{v}_f \phi_f \cdot \vec{A}_f = \sum_{f}^{N_{faces}} \Gamma_\phi (\nabla \phi)_n \cdot \vec{A}_f + S_\phi V \qquad \text{(A.2)}$$

where

N_{faces} = number of faces enclosing cell

ϕ_f = value of ϕ convected through face f

$\rho_f \vec{v}_f \cdot \vec{A}_f$ = mass flux through the face

$\vec{A}_f$ = area of face f

$(\nabla \phi)_n$ = magnitude of $\nabla \phi$ normal to face f

V = cell volume

For the convective term (the one on the left hand side), the face values of ϕ have to be known. However, only the values at the cell centers (c0 and c1 in Figure A.1) are stored by FLUENT. The face values have to be interpolated from the cell values. They are derived from the corresponding "upwind" values, i. e. from the cell values in an upstream direction to the face relative to the direction of the normal velocity. Hence, the approach is known as the *upwind scheme*.

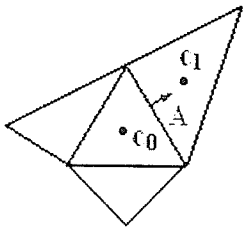

Figure A.2: Part of a computational grid to illustrate the discretization of the general ϕ equation (Fluent, 2001).

In general, the linearized form of (A.2) can be written as

$$a_p \phi_p + \sum_{nb} a_{nb} \phi_{nb} = b_p \tag{A.3}$$

Here, the subscript nb denotes neighboring cells, the subscript p refers to the values in the cell considered, a_p and a_{nb} are the linearized coefficients of ϕ_p and ϕ_{nb}, and the addend b arises from the linearization of the source term. The form of the linearized coefficients depends on the scheme used to interpolate the face values. FLUENT offers different discretization schemes – first-order upwind, second-order upwind, power law, and QUICK. Only QUICK scheme has been applied in the present runs (the interested reader is referred to Fluent (2001) for additional information about the different discretization schemes).

Discretization of the Momentum Equation

An interpolation scheme is required to compute the face values of pressure from the cell values. In the present work, the PRESTO method is used for the pressure discretization. The PRESTO (PREssure STaggering Option) scheme uses the discrete continuity balance for a "staggered" control volume about the face to compute the "staggered" (i.e., face) pressure

Pressure-Velocity Coupling

Pressure-velocity coupling is achieved by deriving an equation for pressure from the discrete continuity equation. The SIMPLE, SIMPLEC, and PISO pressure-velocity coupling methods are available in FLUENT. In the present work, the PISO method is applied for the pressure-velocity coupling. The Pressure-Implicit with Splitting of Operators (PISO) pressure-velocity coupling scheme, part of the

SIMPLE family of algorithms, is based on the higher degree of the approximate relation between the corrections for pressure and velocity. Details of this method can be found in (Fluent, 2001).

REFERENCES

Anderson, T. J., and Uhlherr, P. H. T., 1977, "The influence of stream turbulence on the drag coefficient spheres", *Preprints of papers to the sixth Australian Hydrodynamics and Fluids Mechanics Conference, Australia, Institute of Engineering*, pp. 541-545.

Abou Al-Sood, M., 2006, "A numerical study of a droplet evaporating in a turbulent airflow", Ph. D. thesis, Department of Mechanical and Manufacturing Engineering, University of Manitoba.

Bagchi, P., and Balachandar, S., 2003, "Effect of turbulence on the drag and lift of a particle", *Physics of Fluids*, Vol. 15, pp. 3496-3513.

Birouk, M., and Abou Al-Sood, M., 2007, "Numerical study of sphere drag coefficient in turbulent flow at low Reynolds number", *Numerical Heat Transfer*, part a, Vol. 51, pp. 39-57.

Burcato, A., Grisafi, F., and Montante, G., 1998, "Particle drag coefficients in turbulent fluids", *Chemical Engineering Science*, Vol. 53, pp. 3952-3314.

Clamen, A., and Gauvin, W. H., 1969, "Effect of turbulence on the drag coefficients of spheres in a supercritical flow regime", *IChE, J.*, Vol. 15, pp. 184-189.

Clift, J. R., Grace, J. R., and Weber, M. E., 1978, Bubbles, Drops and Particles, New York: Academic Press.

Constantinescu, G. S., Chapelet, M., and Squires, K. D., 2003 "Turbulence modeling applied to flow over a sphere", *AIAA Journal.*, Vol. 41, no. 9, pp. 1733-1742.

Constantinescu, G. S., Pacheco, R., and Squires, K. D., 2002, "Detached-eddy simulation of flow over a sphere", *AIAA J.*

Constantinescu, G. S., and Squires, K. D., 2004, "Numerical investigation of the flow over a sphere in the subcritical and supercritical regimes", *Physics of Fluids,* Vol. 15, no. 5 , pp. 1449-1467.

Constantinescu, G. S., and Squires, K. D., 1999, "LES and DES investigations of turbulent flow over a sphere", *AIAA J.*,

Constantinescu, G. S., and Squires, K. D., 2003, "LES and DES investigations of turbulent flow over a sphere at Re = 10,000", *Flow, Turbulence and Combustion J.*, Vol. 70, pp. 267-298.

Faldun, E. A., Verzicco, R., Orlandi, P., and Mohd-Yusof, J., 2000, "Combined immersed-boundary finite-difference methods for three-dimensional complex flow simulations", *J. Computational Physics*, Vol. 161, pp. 35-60.

FLUENT User's Guide (2005), *Fluent Inc.*, Lebanon NH 03766, USA.

Fornberg B., 1988, "Steady viscous flow past a sphere at high Reynolds numbers", *J. Fluid Mech.*, Vol. 190, pp. 471-489.

Gilmanov A., Sotiropoulos F., and Balaras E., 2003,"A general reconstruction algorithm for simulating flows with complex 3D immersed boundaries on Cartesian grids", *J. Computational Physics*, Vol. 191, pp. 660-669.

Gore, R. A., and Growe, C. T., 1990, "Discussion of particle drag in a dilute turbulent two-phase suspension flow", *Int. J. Multiphase Flow*, Vol. 16, pp. 359-361.

Harlow, F. H., Nakayama, P. I., 1967, "Turbulence transport equations", *Physics Fluids*, Vol. 10, pp. 2323-2423.

Johnson, T. A., and Patel, V. C., 1999, "Flow past a sphere up to a Reynolds number of 300", *J. Fluid Mech.*, Vol. 378, pp. 19-70.

Kanatha, L. H., 2004, "Length scale equations in turbulence models", *Nonlinear Processes in Geophysics*, Vol. 11, pp. 83-97.

Kim, J., Kim, D., and Choi, H., 2001, " An immersed boundary finite-volume method for simulations of flow in complex geometries", J. Computational Physics, Vol. 171, pp. 132-150.

Kolmogorov, A. N., 1942, "Equations of turbulent motion of an incompressible fluid", *Inz. Akad. Nauk SSSR Ser. Fiz.*, Vol. 6, pp. 56-58.

Kral, L. D., 1998, "Recent experience with different turbulence models applied to the calculation of flow over aircraft components", *Prog. Aerospace Science*, Vol. 34, pp. 481-541.

Mathieu, J., and Scott, J., 2000, "An introduction to turbulent flow", Cambridge University press.

Menter, F. R., 1994, "Two-equation eddy-viscosity turbulence models for engineering applications", *AIAA Journal*, Vol. 32, no. 8, pp. 1598-1605.

Neve, R. S., 1986, "The importance of turbulence macroscales in determining the drag coefficient of spheres", *Int. J. Heat and Fluid Flow*, Vol. 7, pp. 27-36.

Roos, F.W., and Willmarth, W. W., 1971, "Some experimental results on sphere and disk drag", *AIAA J.*, Vol. 9, pp. 285-291.

Rotta, J. C., 1951, "Statistiche Theorie Nichthomogener Turbulenz", Zeitschrift under Physics, bD 129, pp. 547-572.

Rudoff, R. C., and Bachalo, W. D., 1988, "Measurement of droplet drag coefficient in polydispersed turbulent flow field", *AIAA Thermophysics, Plasmadynamics and Laser Conference Proceeding, San Antonio, Texas, USA.*

Spalding, D. B., 1972, "The model of turbulence", Imperial College, Mechanical Engineering Report TM/TN/A/16.

Sundararajan, T., and Ayyaswamy, P. S., 1984, "Hydrodynamics and heat transfer associated with condensation on a moving drop: solution of intermediate Reynolds number", *J. Fluid Mech.*, Vol. 149, pp. 33-58.

Takiguchi S., and Kajishima T., 1999, "Numerical scheme to resolve the interaction between solid particles and fluid turbulence", *JSME International J.*, Vol. 42, no. 3, pp. 411-418.

Torobin, L. B., and Gauvin, W. H., 1961, "Drag coefficients of single sphere moving in steady and accelerated motion in a turbulent fluid", *AIChE, J.*, Vol. 7, pp. 615-619.

Pope, Stephen, 2000, 1st edition" Turbulent Flows", Cambridge University press.

Uhlherr, P., and Sinclair, C., 1970, "The effect of free-stream turbulence on the drag coefficient of freely entrained spheres," *Chemica 70: A conference convened by Australian National Committee of Institution of Chemical Engineers and Australian Academy of science*, pp. 1-13.

Warnica, W. D., Renksizbulut, M., and Strong, A. B., 1995a, "Drag coefficient of spherical liquid droplets; Part 1: Quiescent gaseous fields", *Exp. Fluids*, Vol. 18, pp. 258-264.

Wang, Z. J., and Kannan, R., 2005, "An adaptive Cartesian/Prism grid method for moving boundary flow problems", *AIAA J.*

Yusof, J., 1996, "Interaction of massive particles with turbulence", Ph. D. thesis, Department of Mechanical Engineering, Cornell University.

Zarin, N. A., and Nicholls, J. S., 1971, "Sphere drag in solid rockets-non-continuum and turbulent fluids", *Combustion Science and Technology*, Vol. 3 pp. 273-285.